Atmospheric Environment 205 (2019) 90–102

Contents lists available at ScienceDirect

Atmospheric Environment

journal homepage: www.elsevier.com/locate/atmosenv

Bioavailable iron production in airborne mineral dust: Controls by chemical composition and solar flux

Eshani Hettiarachchi[a], Richard L. Reynolds[b,c], Harland L. Goldstein[b], Bruce Moskowitz[c], Gayan Rubasinghege[a,*]

[a] Department of Chemistry, New Mexico Institute of Mining and Technology, Socorro, NM, 87801, USA
[b] U.S. Geological Survey, Denver, CO, 80225, USA
[c] Institute for Rock Magnetism, Department of Earth Sciences, University of Minnesota, Minneapolis, MN, 55455, USA

GRAPHICAL ABSTRACT

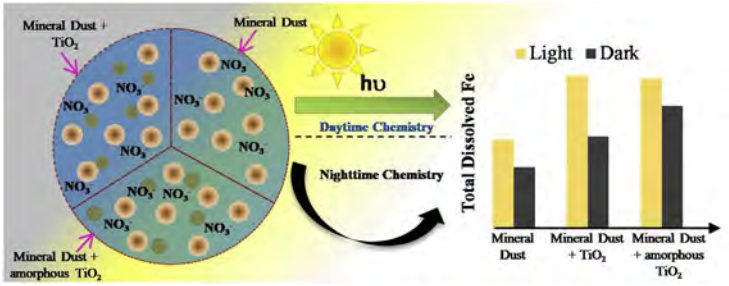

ARTICLE INFO

Keywords:
Bioavailable iron
Iron dissolution
Photochemistry
Mineralogy effects
Redox cycling
Titanium dioxide

ABSTRACT

A large part of oceanic biological production is limited by the scarcity of dissolved iron. Mineral dust aerosol, processed under acidic atmospheric conditions, is the primary natural source of bioavailable iron to oceanic life. However, synergistic and antagonistic effects of non-Fe-containing minerals on atmospheric processing of Fe-containing minerals and Fe solubilization are poorly understood. The current study focuses on mineralogical influences of non-Fe-bearing semiconductor minerals, such as titanium dioxide (TiO_2), on the dissolution of iron in selected natural mineral dust aerosols under atmospherically relevant conditions. Further, the role of elevated Ti concentrations in dust is evaluated using magnetite, a proxy for Fe(II) containing minerals, under both dark and light conditions. Our results highlight that relatively higher Ti:Fe ratios, regardless of their total Fe content, enhances the total iron dissolution in mineral dust aerosols as well as in magnetite. Moreover, elevated Ti percentages also yield high Fe(II) fractions in mineral dust systems under dark conditions. Upon irradiation however, dissolved Fe(II) is suppressed by high Ti levels due to the involvement of photochemical redox cycling reactions with hydroxyl radicals (˙OH). These synergistic and antagonistic effects of Ti are further evaluated by altering the chemical composition of natural dusts with artificially added anatase (TiO_2) and synthetic amorphous titania. The current study reveals important mineralogical controls by non-Fe-bearing minerals on dust iron dissolution to better understand global iron mobilization.

* Corresponding author.
E-mail addresses: eshani.hettiarachchi@student.nmt.edu (E. Hettiarachchi), rreynolds@usgs.gov (R.L. Reynolds), hgoldstein@usgs.gov (H.L. Goldstein), bmosk@umn.edu (B. Moskowitz), gayan.rubasinghege@nmt.edu (G. Rubasinghege).

https://doi.org/10.1016/j.atmosenv.2019.02.037
Received 7 November 2018; Received in revised form 19 February 2019; Accepted 21 February 2019
Available online 01 March 2019
1352-2310/

1. Introduction

Phytoplankton are at the base of almost all marine food webs, and are a major sequesterer of atmospheric carbon dioxide (CO_2) at a global scale (Rubasinghege et al., 2010; Borgatta et al., 2016; Li et al., 2017; Pabortsava et al., 2017). Although phytoplankton growth is expected to correlate with ocean macronutrient content, approximately 30% of the world's oceans behave otherwise. Some large regions, including Equatorial Pacific, Subarctic North Pacific, and Southern Ocean, have low phytoplankton biomass despite high nitrate levels throughout the year. Such areas are known as high-nitrate-low-chlorophyll (HNLC) regions (Tyrrell et al., 2005). Among several possible reasons for these surprisingly low chlorophyll levels, is the limitation of the micronutrient, iron. While iron is an important trace element for the metabolism and growth of all organisms, it is an essential nutrient for phytoplankton due to its presence in iron–sulfur and cytochrome proteins involved in photosynthetic electron transport (Erdner and Anderson, 1999). Iron dissolution from the Earth's crust in seawater is limited due to the oxic ocean pH (~ 8.2) (Stefánsson, 2007). Hence, atmospheric processing of iron-containing aerosols followed by their deposition with solubilized iron on surface water has been suggested as a source of bioavailable Fe to oceans (Martin, 1990). In addition to this "Fe hypothesis," light limitation and grazing pressure are also identified as additional factors that limit phytoplankton growth in HNLC regions (De Jong et al., 2012). Apart from oceans, Fe is also important as a limiting nutrient (usually less than 1 ppm) for the growth of freshwater algae and aquatic plants (Xing et al., 2011). In freshwater lakes, moreover, variations in available Fe concentrations can influence microbial composition. These studies further report that even small differences in Fe concentrations; i.e., 0.1 ppm vs. 1 ppm, can trigger significant shifts in the microbial community in lakes from green algae to cyanobacteria (Xing et al., 2011). In addition to aeolian transport, freshwater lakes may get dissolved iron from soil and sediments around the lakes through groundwater and rivers. Therefore, it is important to understand iron supply to both freshwater bodies and oceans.

Among the sources of iron contained in tropospheric aerosols, mineral dust, fly ash, and volcanic ash are dominant (Frogner et al., 2001; Chen et al., 2012a; Chen et al., 2013; Bhattachan et al., 2016; Borgatta et al., 2016; Lu et al., 2017). Iron-rich mineral dust physically and chemically interacts during transport with other atmospheric components in the acidic aqueous deliquescent layer formed around a dust particle by the uptake of water vapor and acidic gases (Mahowald et al., 2005; Rubasinghege et al., 2010). Acidic conditions in the atmosphere may overcome the buffer capacity of mineral dust particles, dropping the pH of this deliquescence layer as low as 1 to 2 (Desboeufs et al., 2003; Meskhidze et al., 2005; Fu et al., 2010). In general, aerosols influenced by anthropogenic air masses have shown such low buffer capacities (Ingall et al., 2018). One such abundant acidic atmospheric gas is nitric acid that is primarily generated from gaseous nitrogen oxides (Gankanda et al., 2014). Among many Fe-bearing minerals, hematite (α-Fe_2O_3) has been well studied and considered as an important iron source owing to its abundance and contribution to the total Fe in mineral dust. However, numerous previous studies have reported that other Fe-containing minerals, i.e. goethite (α-FeOOH), magnetite (Fe_3O_4), ilmenite ($FeTi_2O_3$), ferrihydrite ($Fe_5HO_8{\cdot}4H_2O$), and many structural iron substituted clays, may also contribute to bioavailable iron (Formenti et al., 2003; Kandler et al., 2007; Wu et al., 2007; Shi et al., 2009, 2012; Reynolds et al., 2014a; Moskowitz et al., 2016). Moreover, these studies discuss that the rate and extent of iron dissolution depend on several factors, including particle properties such as size, crystallinity, Fe content, as well as environmental properties, such as pH, temperature, availability of sunlight, and humidity (Zhu et al., 1993; Fu et al., 2010; Rubasinghege et al., 2010; Paris et al., 2011; Wijenayaka et al., 2012; Hettiarachchi et al., 2018a,b). Apart from the natural mineral dust aerosol, it has been hypothesized that Fe bearing minerals such as magnetite from anthropogenic sources can be transformed to bioavailable iron during the atmospheric transport (Ito et al., 2018). Field observational data show magnetite in anthropogenic aerosols ubiquitously (Moteki et al., 2017; Ohata et al., 2018; Yoshida et al., 2018). However, laboratory simulation suggests slow iron dissolution from magnetite at atmospherically relevant low pH (Journet et al., 2008).

The phase compositions of mineral dust are rather complex to mimic by a single mineral phase. Highlighting the vital role of mineral phases in iron dissolution, Journet et al. (2008) reported that structural iron in clay particles are more mobile compared to that of single component iron oxides (e.g. hematite). Cwiertny et al. (2008) in their studies with natural dust and commercial dusts further showed that iron dissolution does not necessarily correlate with Fe concentrations or the surface area of the dust samples. Instead, Fe(II) containing solid phases, such as Fe-substituted aluminosilicates, showed a significantly high Fe solubility in acidic environments (Cwiertny et al., 2008). A similar study done by Fu et al. (2010) previously concluded that Fe-containing Arizona Test Dust (AZTD) particles were more soluble than Inland Saudi Sand (IS) and Saharan Sand (SS) samples regardless of experimental conditions. They further discussed that the AZTD contained higher content of clay minerals whereas the IS and SS samples are rich in rather non-reactive quartz sand. Our recent work on a Fe-bearing oxide, ilmenite, reported higher Fe dissolution compared to that of single component Fe-oxides (Fe_2O_3), despite its relatively lower Fe abundance (Hettiarachchi et al., 2018a,b). These studies of aeolian sediments thus suggest that the mineralogy of the Fe-bearing mineral phase has a strong influence on iron dissolution.

Mineral dust compositions are complex; Fe-bearing minerals are well mixed with non-Fe-containing metal oxides. For example, Ca, Mg, K, Na and Ti are also found in dust particles as oxides and carbonates (Kruegner et al., 2004; Kandler et al., 2007; Shao et al., 2007). The dissolution of iron from hematite and other Fe bearing oxides in mineral dust mainly follows three mechanisms: proton-promoted, ligand-controlled, and reductive dissolution. These mechanisms involve adsorption of anionic ligands (e.g. acid anion or organic anion) onto Fe-bearing mineral surfaces that weakens the bonds of surface Fe atoms leading to detachment of Fe into the deliquescent layer (Wiederhold et al., 2006; Rubasinghege et al., 2010; Li et al., 2017; Wang et al., 2018; Biswakarma et al., 2019; Kang et al., 2019). A large quantity of non-Fe-bearing metal oxides in mineral dust allows for them to compete for acid and/or organic anions in the deliquescent layer and, thus, to influence iron dissolution. Previous studies on gas-solid interactions report that adsorption of acid anions onto mineral dust components such as Al_2O_3 and TiO_2 results in solvated ions under humid conditions (Goodman et al., 2001; Gankanda et al., 2014). Moreover, some of these interactions may even yield secondary products that passivate or activate the dust surface or modify crystal phases. Such modifications can affect the Fe-bearing mineral dust surface, thereby altering its dissolution (Henderson, 2003; Grybos et al., 2010; Henderson, 2011). Furthermore, some non-Fe-containing components in mineral dust are semi-conductors (e.g. TiO_2) having wide band gaps that possess the capacity to generate hydroxyl radicals ($^{\bullet}OH$) from surface-adsorbed-water upon irradiation (Zhang et al., 2014). These photochemical reaction pathways may further influence iron dissolution and its speciation.

Biogeochemical modeling plays an important role in understanding the present day biogeochemical properties and processes in the ocean that can be used to predict possible future responses to disturbances resulting from human activities. For this application, the models need substantial improvements that cover the complexities and applications in the global biogeochemical systems. However, current atmospheric models are incapable of accommodating these complexities (Doney et al., 2001; Held, 2005; Lohmann et al., 2007; Jackson et al., 2015; Myriokefalitakis et al., 2018). The total iron source in current models is limited to hematite. One limitation to accommodate complex interactions among many different aerosols is the poor understanding of

synergistic and antagonistic effects of non-Fe-containing minerals on Fe solubilization and speciation. In the current study, we discuss the dependence of iron dissolution and speciation in mineral dust aerosols on solar flux and on aerosol chemical composition, in particular the effect of Ti. Here, we evaluate the dissolution of Fe from four natural dust samples, and one Fe-bearing mineral dust proxy, magnetite ($FeO.Fe_2O_3$) along with a common Ti-bearing mineral in mineral dusts, TiO_2. Our results highlight that the presence of Ti in mineral dusts enhances the total Fe dissolution under both dark and light conditions, regardless of their Fe concentrations, dust surface area, or Fe-bearing mineral phases.

2. Materials and methods

2.1. Materials

2.1.1. Natural dust sample collection

Three of the four analyzed dust samples were derived from surface sediments in dust-source areas that were subsequently sieved to sizes representative of dust particles emitted from the respective areas. The fourth sample represents true dust having source area as much as ~400 km distant. We refer to these samples collectively as natural dust samples. Sample BK1 was collected from a dune in the Kalahari Desert, Botswana, Africa (−28.88, 20.7) (Bhattachan et al., 2012) and sieved to 45 μm. The Stop15 sample was collected from surface sediment in the Chinle Valley, Arizona (36.70420, −109.88877) and sieved to 63 μm. The TF3 sample was collected from surface sediment in the Little Colorado River corridor, Arizona (35.14267, −110.71247) and sieved to 20 μm. The sample SASP was collected from dust deposited on snow near Red Mountain Pass, San Juan Mountains, Colorado (37.9069, −107.7114) and is a composite of the majority of dust deposited from October 2008 through May 2009 from nearby (< 500 km) sediment sources areas in Arizona (Chinle Valley, Little Colorado River corridor) and New Mexico. According to dominant wind patterns, global dust cycle distribution and observations of satellite imagery, the Kalahari Desert dust (BK1) is more likely to deposit on the Southern Atlantic Ocean, whereas the two samples from dust sources in the American Southwest travel predominantly to the northeast and likely deposit on freshwater lakes and mountain snowpack (Mahowald et al., 2005; Zhang et al., 2016, 2018). Some finer particles of southwestern-derived dust may be transported farther east over North American industrial regions where they may interact with gaseous nitrogen oxides, thereby becoming acid-processed before deposition.

2.1.2. Standard samples and reagents

All chemicals were reagent grade or better and were used as received. All the solutions were prepared in Milli-Q water (18MΩ, Milli-Q Advance 10). Hydroxylamine hydrochloride (NH_2•OH•HCl, Acros Organic, 99%), ammonium fluoride (NH_4F, Baker Chemicals, 99%), concentrated hydrochloric acid (HCl, Scholar chemicals, 36%), ammonium acetate (CH_3COONH_4, Mallinckrodt, 99%), acetic acid (CH_3COOH, VWR International, glacial), 1,10-phenanthroline ($C_{12}H_8N_2$, Acros organics, 99 + %), and ferrous ammonium sulfate hexahydrate ($Fe(NH_4)_2(SO_4)_2$•$6H_2O$, Fischer Scientific, 98.5%) were used during the analysis of dissolved iron based on the procedure previously described in Stucki et al. (1981). The dissolution studies were also carried out using selected mineral dust proxies, i.e., anatase (TiO_2, Degussa, 99%) and magnetite ($FeO.Fe_2O_3$, W041183, Wright industries, Brooklyn, NY). Magnetic and Mossbauer analysis indicate W041183 is virtually pure, stoichiometric magnetite (Cater-Stiglitz et al., 2006). The effects of the crystallinity of TiO_2 on Fe dissolution from mineral dust proxies were briefly tested with a synthesized sample of amorphous titania. The details of synthesis are provided in Text S1 in supporting information.

2.2. Sample characterization

The shape and size of mineral particles were determined from single particle analyses with scanning electron microscope (SEM) and transmission electron microscopy (TEM). The particles were suspended in isopropyl alcohol and transferred onto a sample holder. The samples were sputter coated with platinum (Pt) prior to analysis. The size distribution was determined by analyzing ~800 particles using the software package ImageJ (version 1.50i). Surface areas of mineral samples were measured in a seven-point N_2-Brunauer-Emmet-Teller (BET) isotherm using a Quantachrome Autosorb-1 surface area analyzer. Samples were outgassed overnight (~24 h) at a temperature of 105 °C prior to the BET analysis. Major, minor and trace elements were determined using inductively coupled plasma-atomic emission spectroscopy (ICP-AES) following a 4-acid digestion method (Briggs, 2002). Mineral identifications were determined using powder X-ray diffraction (XRD) techniques, reflection spectroscopy, magnetometry, and Mössbauer spectroscopy. Further, more labile Fe phases were quantified using the hydroxylamine HCl/acetic acid extraction method described in Poulton et al. (2005) and references therein. XRD mineral data were collected using copper Kα radiation using a Philips XRG 3100 and a Norelco goniometer equipped with a graphite monochromator. Identifications were facilitated using JADE software by Materials Data, Inc. Reflectance spectroscopy was performed using an Analytical Spectral Devices Inc. FieldSpec3 spectrometer, covering the wavelength range of 0.35–2.50 μm in 2151 channels. A bidirectional reflectance measurement setup was used, with the light source and the fiber optic head of the spectrometer at fixed angles above the sample. The mineral compositions of samples were characterized by analyzing their reflectance spectra and comparing to reference spectra of minerals and other materials in the USGS spectral library (version 6; Clark et al., 2007). Mössbauer spectroscopy and magnetometry were carried out on powdered samples (~100 mg) at the Institute for Rock Magnetism (IRM), University of Minnesota, USA. Mössbauer spectra were measured at 4.2 K and 300 K using a conventional constant-acceleration spectrometer equipped with a Nitrogen shielded Helium dewar in transmission geometry with a ^{57}Co/Rh source. An α-Fe foil at room temperature was used to calibrate isomer shifts and velocity scale. Mössbauer spectra were fit using the NORMOS program (Brand, 1987). Magnetization measurements were made using a vibrating sample magnetometer (Princeton Corporation Measurements) and a SQUID magnetometer (Quantum Design, San Diego, CA, USA – MPMS-XL).

The band gaps of magnetite and anatase were measured according to a solution-phase method previously described by D'Souza et al. (2013). Anatase and magnetite suspensions were prepared in Milli-Q water and pH 5 ammonium acetate buffer. For the magnetite suspension, the buffer solution was used to prevent particle aggregation of magnetite in Milli-Q water. The band gap measurement of magnetite particles of interest is necessary because it is highly dependent on particle size (El Ghandoor et al., 2012).

2.3. Dissolution experiments

Batch reactor studies simulate the acidic deliquescence layer of mineral dust particles, formed by heterogeneous uptake of atmospheric acidic gasses such as nitric acid, sulfuric acid, organic acids, and gaseous water. As described above, highly acidic atmospheric conditions can produce a deliquescence layer with very low pH values such as 1 or 2 (Cwiertny et al., 2008; Ingall et al., 2018). These studies were carried out to measure dissolved iron using custom-built glass reactors, described in our previous studies (Hettiarachchi et al., 2018a-b). Briefly, the reaction vessel has a suspension capacity of 100 mL with a removable airtight top. In all experiments, the particle loading was ~0.2 g/L of the mineral dust in acid solutions at pH 2. When mixtures were analyzed, their masses were adjusted to achieve a final loading of 0.2 g/L. Prior to dissolution experiments, the acid solutions were

purged with nitrogen gas at 5 sccm (standard cubic centimeters per minute) for 5 min to obtain a reduced atmosphere. Reduced atmosphere was simulated in order to study the mechanistic pathways arising from the particle properties and anions. The effect of oxygen is suggested for future studies. The experiments were performed in the presence and absence of simulated solar radiation (150 W xenon lamp, Newport Sol1A Class ABB Solar Simulator). A quartz window (12.5 cm^2) mounted on the top allowed the entry of light during the solar experiments. The solution surface receives a solar flux of ~105 mW/cm^2, and this flux remains constant throughout the light experiments. These glass reactors were also equipped with a temperature probe and a standardized pH electrode to measure these parameters throughout the dissolution experiments. Temperature was kept constant at 25 °C through the use of a water jacket. During the dissolution experiment, the suspension was agitated constantly to mimic the mixing in the deliquescent layer. Over time, samples were periodically removed from the reactor using a disposable syringe that was connected to 12 cm Teflon tubing. The collected samples were filtered through 0.2 μm filters and analyzed using the 1,10-phenanthroline method (Stucki et al., 1981). All the batch reactor studies were triplicated. The mean dissolved iron concentrations with one standard deviation are reported.

3. Results and discussion

3.1. Particle characterization

3.1.1. Morphology, particle size, and surface area

Surface characterization of particles provides important information about their morphology. The natural dust samples and dust proxies differ in their shapes and particle sizes from one another as illustrated by SEM and TEM images (Fig. 1). The four natural dust samples, Stop15, SASP, TF3, BK1, and magnetite were irregular in shape with aspect ratios ranging from 1.6 to 2.3 whereas that of anatase was closer to 1, indicating more spherically shaped particles (Podczeck, 1997). The average particle sizes of the natural dust samples ranged from a few micrometers to a few hundreds of micrometers, as measured using SEM images, and were 33 ± 8 μm, 42 ± 2 μm, 88 ± 53 μm and, 8 ± 2 μm for Stop15, BK1, SASP, and TF3, respectively. The particle sizes of anatase (calculated using TEM images) and magnetite (from SEM images) were 25 ± 3 nm and 19 ± 7 μm, respectively. The magnetite particle size is consistent with previous measurements (Yu et al., 2002). The SEM image of SASP particles revealed their aggregated nature. The specific surface areas of dust samples were 12 ± 1 m^2g^{-1}, 114 ± 4 m^2g^{-1}, 6 ± 1 m^2g^{-1} and 63 ± 1 m^2g^{-1} for Stop15, BK1, SASP, and TF3 samples, respectively, whereas those of magnetite and anatase were 1.8 ± 0.2 m^2g^{-1} and 59 ± 2 m^2g^{-1}.

3.1.2. Elemental composition analysis and mineral-phase identification

Information on chemical compositions, mineral phases, and crystallinity, is vital to assess iron mobility in mineral dust aerosols. According to ICP-AES analysis, Fe mass concentrations in TF3, BK1, Stop15, and SASP were 3.63%, 3.51%, 3.03% and 2.18%, respectively (Table 1).

All four natural dust samples contained hematite, goethite, and low amounts of magnetite as identified with Mössbauer spectroscopy and magnetometry. No indication of ferrihydrite was detected. Hematite and goethite accounted for 56%, 53%, 52%, and 64% of total Fe content in SASP, TF3, Stop15 and BK1, respectively. The contributions of magnetite to the total Fe content were 2.7%, 0.6%, 0.24% and 2.3% for the SASP, TF3, Stop15, and BK1 samples, respectively, whereas the remaining Fe occurred as Fe(III) and Fe (II) in other Fe-containing mineral phases such as clay. The Fe(II) Mössbauer subspectral doublet accounts for 10%, 8%, 10%, and 7% of the total spectral area for SASP, TF3, Stop15, and BK1, respectively. Therefore 90–93% of the iron is Fe (III) in our dust samples. The mineral phases identified by XRD and reflectance spectroscopic results, are provided in Tables S1–S4 in Supporting Information. Further, the amounts of labile Fe phases were negligible compared to the other iron phases, and there was no significant difference among the selected dust samples. (Table S5 in Supporting Information). Moreover, the chemical composition of these samples were also analyzed in three size fractions, PM_{10}, PM_{20}, and PM_{63}, and found no significant variations ($p > 0.05$) based on the particle size.

3.1.3. Band-gap measurements

The measured band gaps of magnetite and anatase were 2.88 ± 0.03 eV (~430 nm) and 3.16 ± 0.02 eV (~392 nm), respectively, and are classified as wide band-gap semiconductors (Kurniawan et al., 2018). The semiconductor oxides with wide band gaps such as anatase possess the capability of being activated under UV irradiation to generate hydroxyl radicals from surface-adsorbed water (Zhang et al., 2014). Apart from $^{\bullet}OH$, TiO_2 surfaces may form nitrate derived radicals from the adsorbed nitrates in mineral dust (Gankanda et al., 2014; Lesko et al., 2015). Characterization results of synthesized amorphous titania are provided in Fig. S1(b) and Table S6 in Supporting Information.

3.2. Batch reactor studies - iron dissolution measurements

3.2.1. Dissolution of Fe-bearing minerals and controls by chemical composition of dust

3.2.1.1. Total dissolved iron. The selected mineral dust samples exhibited large variations in their rates and extents of total iron dissolution under both dark and light conditions (Fig. 2). The dissolution data were fitted to a Langmuir-type model to derive pseudo first order rates (Table 2). Under dark conditions, these initial rates were 8 ± 2 $\mu M\, g^{-1}\, hr^{-1}$, 16 ± 1 $\mu M\, g^{-1}\, hr^{-1}$, 18 ± 2 $\mu M\, g^{-1}\, hr^{-1}$, and 53 ± 3 $\mu M\, g^{-1}\, hr^{-1}$ for SASP, BK1, Stop15, and TF3, respectively. However, the mass normalized extents of total iron dissolution after 48 h of reaction increased on the order of SASP < BK1 < TF3 < Stop15 respectively at the end of the 48th hour. (Fig. 2(a). Such discrepancies can be expected due to the differences in total Fe content and specific surface areas of mineral dust particles. Lower dissolution rates and surface area measurements of the SASP sample could be due to surface passivation during its previous atmospheric processing and/or weathering. However, this seems unlikely because the Fe concentration of the SASP sample is consistent with Fe concentrations in source area sediments indicating that Fe concentration in the dust sample has been inherited from the source materials. Furthermore, the dust sample (San Juan Mountains, Colorado) was transported quickly from nearby source areas in Arizona and New Mexico, on the order of < 1 day, so there was little time from any atmospheric processing. To eliminate surface area effects, these results were normalized to their respective surface area (Fig. 2(b)). On a surface area basis, the extent of total iron dissolution after 48 h in the Stop15 sample was at least 4-fold higher than those of other dust samples. Moreover, these differences started to appear in the early stages of dissolution. Regardless of the lower total iron concentration, sample SASP had the second highest total iron dissolution followed by those in samples TF3 and BK1. Therefore, total Fe dissolutions of the four natural dust samples do not correlate with their respective total Fe concentrations (Fig. S2(a)).

As previously discussed, the dissolution of iron from mineral dust, and the subsequent distribution of bioavailable iron depend on several factors related to both the dust particles themselves and their environments. Among many other particle properties, the mineralogy of the Fe-bearing solid phases and non-Fe-containing minerals in the mineral dust mixture could play a vital role during this process (Cwiertny et al., 2008; Journet et al., 2008; Hettiarachchi et al., 2018a-b). The % total Fe solubility from the current study is provided in Fig. S6(a) and Table S8 in Supporting Information along with total Fe solubilities observed by other researchers (Cwiertny et al., 2008; Journet et al.,

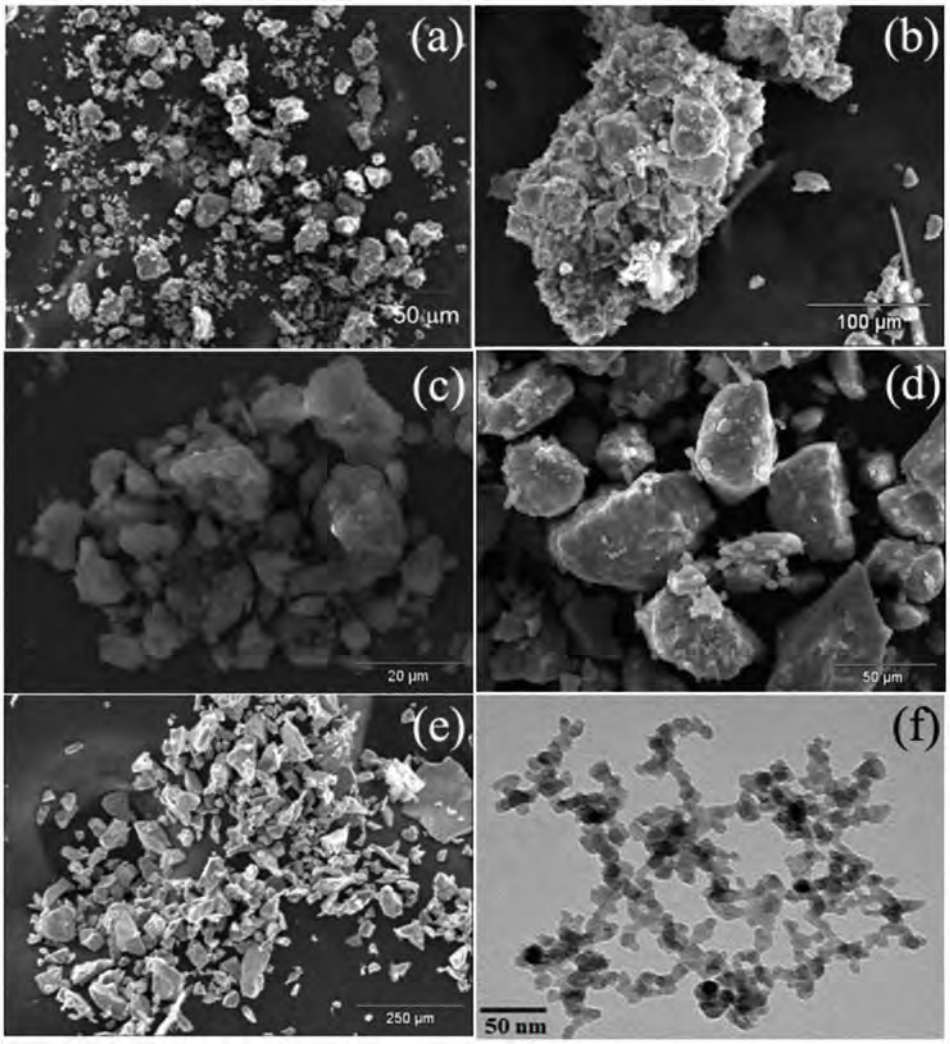

Fig. 1. The SEM images of samples (a) Stop15, (b) SASP, (c) TF3, (d) BK1, (e) Magnetite, and TEM image of (f) anatase samples.

Table 1
Major element concentrations in natural dust samples from ICP-AES analysis.

Sample	Al%	Ca%	Fe%	K%	Mg%	Na%	P% X 10^{-2}	Ti%
SASP	5.71	1.65	2.18	2.18	1.19	1.04	9.10	0.298
TF3	8.49	4.36	3.63	2.47	1.87	0.368	6.89	0.321
Stop15	8.27	4.23	3.03	1.82	1.16	0.272	5.65	2.96
BK1	5.47	0.617	3.51	1.45	0.392	1.31	2.47	0.832

2008; Fu et al., 2010). Although these studies highlight the dependency of Fe solubility on minerology, a direct comparison of the solubility values among these studies is challenging due vast differences in their experimental conditions, i.e. initial pH, availability of oxygen. Based on Mössbauer measurements, the fractions of hematite and goethite minerals in the dust samples in the study varied little between 52 and 64%. Thus, the small differences in the amounts of these Fe oxide minerals cannot explain the large variations in enhanced total Fe dissolution under dark conditions. Moreover, given the negligible amounts of highly labile Fe phases in the selected dust samples, the variations in Fe dissolution could not be due to Fe phases such as ferrihydrite or lepidocrocite. On the other hand, elemental analysis of these dust samples indicate a higher Ti:Fe ratio of 0.98 for Stop15 sample compared to that of other samples; SASP(0.14), BK1(0.24), and TF3(0.09). This highlights a correlation between total dissolved iron and presence of Ti (Fig. S2(b)), and thus suggests possible metal-metal synergistic effects on iron dissolution.

Previous studies have shown that solar radiation increases total iron dissolution in simple iron oxides such as hematite or goethite (Zhu et al., 1993; Rubasinghege et al., 2010). However, natural dust mixtures do not always follow similar trends, especially in low pH environments (Fu et al., 2010). This behavior could be related to the influence of minerals other than Fe-containing oxides in the deliquescent layer. Total iron dissolution under light conditions decreased on a mass-normalized basis for the samples Stop15, BK1, and TF3 by about 1.5, 3, and 4-fold, respectively, as compared to their dark condition counterpart (Fig. 2(a) and (c)). However, under light conditions, the SASP sample showed a 2-fold increase in total dissolved Fe compared to dark conditions. The pseudo first-order rates of total iron dissolution, derived from Langmuir-type model, were $44 \pm 1\,\mu M\,g^{-1}\,hr^{-1}$, $18 \pm 2\,\mu M\,g^{-1}\,hr^{-1}$, and $15 \pm 2\,\mu M\,g^{-1}\,hr^{-1}$ for the Stop15, SASP, and TF3 samples, respectively (Table 2). In sample BK1, iron dissolution was first measurable after approximately 18 h of reaction time. Hence, the kinetics of the initial dissolution could not be determined. Moreover, the highest iron dissolution was still observed for the Stop 15 sample upon irradiation, on both per mass basis and per surface area basis. These results could be, partly or wholly, due to its relatively high Ti concentration and, if so, consistent with the hypothesis for the dark condition; the total Fe dissolution may be enhanced by elevated Ti concentrations–the "Ti hypothesis."

Titanium primarily occurs in mineral dust as TiO_2 (anatase and

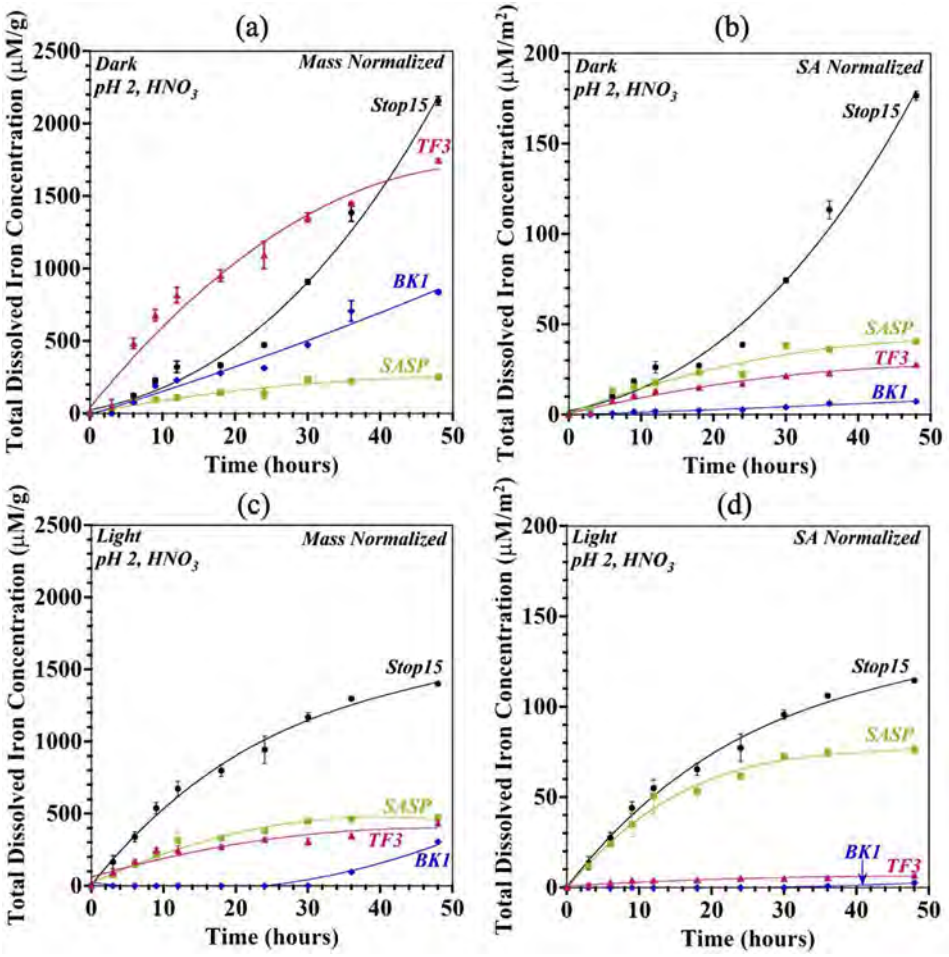

Fig. 2. Total iron dissolution from the four dust samples at pH 2 nitric acid in dark and light. Mass normalized total iron (a) in dark (c) in light and surface area normalized total iron (b) in dark and (d) in light as a function of time. The data have been fitted to a Langmuir-type model.

rutile), ilmenite, Ti-bearing magnetite, and Fe-Ti oxide minerals of the pseudobrookite series (Van Gosen et al., 2018). Titanium especially as TiO_2 is concentrated in the fine fraction of mineral dust. Such fines can undergo long-distance transport, and can thereby be processed under long-duration acidic conditions before deposition (Kandler et al., 2007). In addition to natural occurrences, manmade TiO_2 nanoparticles can be found in the atmosphere and these particles may contribute to the mineral dust (Chen et al., 2012b). To further test and evaluate the titanium hypothesis mentioned above, the natural dust sample TF3 was artificially mixed with TiO_2, to bring its Ti:Fe ratio to that of the Stop15 sample. Here, we selected sample TF3 because it is compositionally similar to sample Stop15, except that Stop15 contains considerably higher Ti content. It is important to mention that XRD analysis of TiO_2, used in dissolution experiments, confirmed no other mineral phases present (Fig. S1(a) in Supporting Information). Moreover, the blank dissolution experiments (control) carried out with only TiO_2 under both dark and light conditions further confirmed that TiO_2 does not contain any labile Fe that contribute to the dissolved Fe. A comparison of iron dissolution and speciation for TF3 and "TF3 + TiO_2" is shown in Fig. 3. Compared to TF3, the total iron dissolution under dark and light conditions for "TF3 + TiO_2" increased about 1.5- and ~5.5-fold, respectively (Fig. 3(a) and (c)). The pseudo first-order rates of total iron dissolution for the TF3 + TiO_2 in dark and light were 73 ± 2 μM g^{-1} hr^{-1} and 49 ± 3 μM g^{-1} hr^{-1}, respectively.

Table 2
Initial rates of the total iron dissolution, determined from Langmuir type model, for all the dust samples and model systems under pH 2 nitric acid in both dark and light. Both mass normalized, μM g^{-1} hr^{-1}, and surface area normalized, μM m^{-2} hr^{-1}, rates are presented. Surface area normalized rates are given within parenthesis.

Sample	Total Iron Dissolution		Surface Area (m^2/g)	Total Fe%
	Dark	Light		
Stop15	18 ± 2 (1.5 ± 0.2)	44 ± 1 (3.6 ± 0.1)	12 ± 1	3.03
BK1	16 ± 1 (0.14 ± 0.01)	n.d. (n.d.)	114 ± 4	3.51
SASP	8 ± 2 (1.3 ± 0.3)	18 ± 2 (3.0 ± 0.2)	6 ± 1	2.18
TF3	53 ± 3 (0.84 ± 0.05)	15 ± 2 (0.24 ± 0.03)	63 ± 1	3.63
TF3 + TiO_2	73 ± 2 (1.6 ± 0.03)	49 ± 3 (0.78 ± 0.05)	(TiO_2 = 59 ± 2)	N/A
Magnetite	82 ± 4 (48 ± 2)	246 ± 5 (145 ± 3)	1.8 ± 0.2	72.4
Magnetite + TiO_2	241 ± 2 (142 ± 1)	551 ± 3 (324 ± 2)	N/A	N/A

N/A: Not Available.

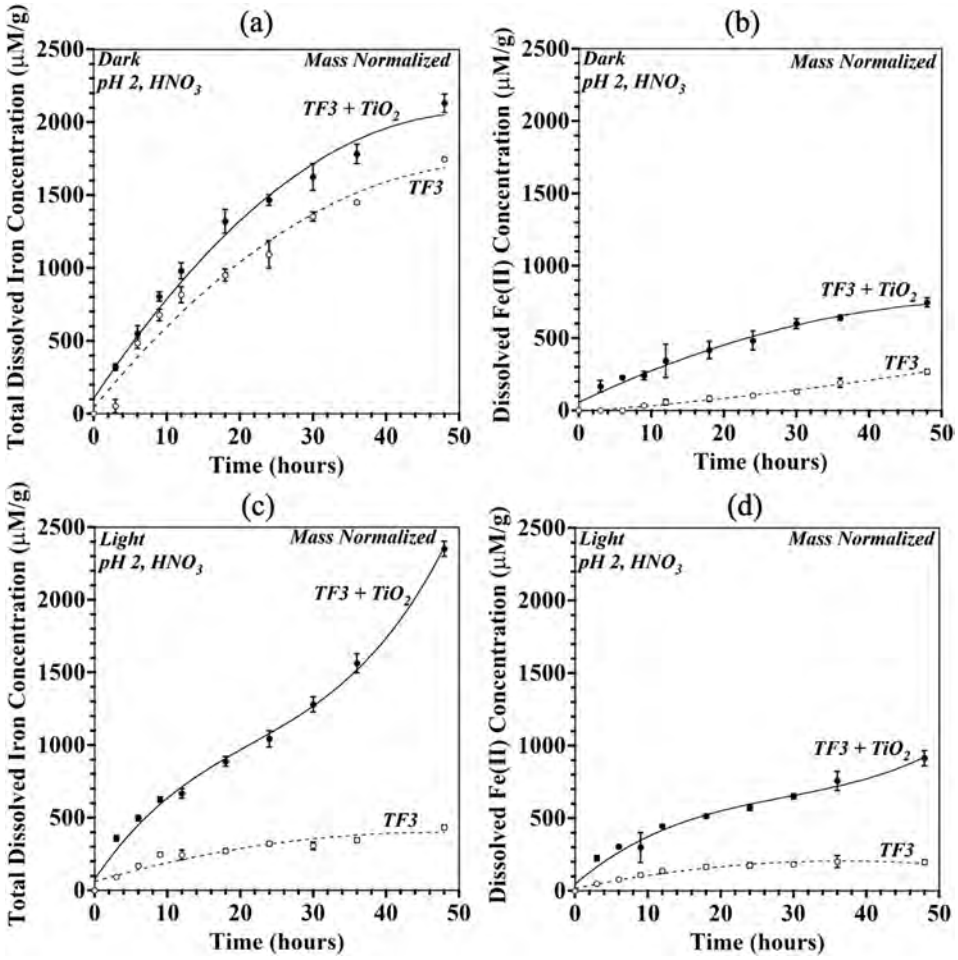

Fig. 3. A mass-normalized comparison of the dissolution of total iron and Fe(II) as a function of time from TF3 and TF3 with added TiO_2 (anatase). (a) Total iron in dark (b) Fe(II) concentration in dark (c) total iron in light (d) Fe(II) concentration in light. The data have been fitted to Langmuir-type model.

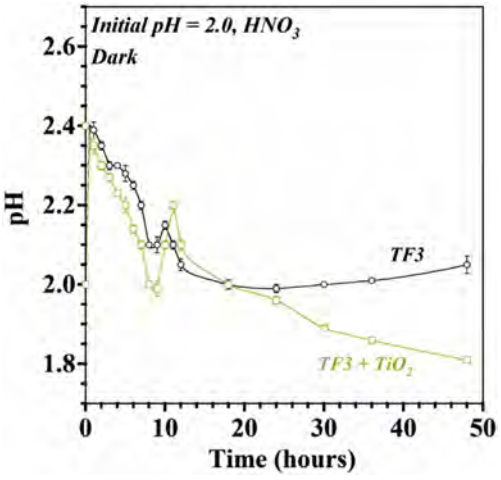

Fig. 4. The pH variation of TF3 and TF3 with added TiO_2 as a function of time.

Heterogeneous uptakes of acidic gases and water vapor on mineral dust surfaces subsequently yield a deliquescent layer with low pH (Rubasinghege et al., 2010). The steady-state pH of this deliquescent layer depends on acid-base chemistry of the mineral dust components in which the adsorbed acid is first titrated with the basic minerals (Goodman et al., 2001; Rubasinghege et al., 2010; Nenes et al., 2011). As an amphoteric oxide, TiO_2 has been shown to interact with gas-phase and solution-phase nitrates (Goodman et al., 2010; Gankanda et al., 2014; Lesko et al., 2015). Under dark conditions, TF3 + TiO_2 showed a noticeably lower pH, especially during the last 30 h of the reaction, compared to just TF3 (Fig. 4). Thus, it is apparent that the enhanced total Fe dissolution in the presence of TiO_2 is promoted by lowering the pH of the suspension. Protons (H^+) generated from Ti (III)/$TiO_{2(hydrated)}$ redox couple could be a probable reason for the observed pH drop (Bard et al., 1985). However, the mechanisms behind lowering the medium pH in these conditions are unclear and are a suggested topic for future studies.

The enhancement of total iron dissolution in "TF3 + TiO_2" sample is greater upon irradiation than that under dark conditions. Further, this difference is more apparent from the beginning of the reaction implying the possibility of other chemical and photochemical reactions occurring in addition to the decreasing pH in the medium. Photoreductive dissolution is a series of photochemical reactions initiated by electron-hole pairs (e^-/h^+) generated on the semi-conductor surface. The Fe(III) in Fe-bearing minerals is reduced to Fe(II) by these photo-excited electrons (e^-) in the conduction band and is detached from bulk, thus enhancing the total iron dissolution. The total iron dissolution is further enhanced when adsorbed water or hydroxyl groups are oxidized by the positively charged holes (h^+) (Wiederhold et al., 2006; Fu et al., 2010; Rubasinghege et al., 2010). The exact role of TiO_2 in the current study is unclear, but it is well known to photo-catalytically produce hydroxyl radicals ($^{\bullet}OH$) from adsorbed water. These radicals then react readily with HNO_3 and NO_3^- forming other reactive oxygen species (ROS), which may enhance total iron dissolution via photochemical reactions (Brown et al., 2001; Nakamura et al., 2004; Shkrob et al., 2011; Zhang et al., 2014). Gankanda et al. (2014) has suggested that higher rates of

nitrate photochemistry on semi-conductor mineral dust surfaces yield relatively high concentrations of NO_2 from adsorbed nitrate (Gankanda et al., 2014). In later studies, preferential reduction of adsorbed nitric acid and formation of nitrous acid on TiO_2 were reported (Lesko et al., 2015). These previous studies suggest chemical and photochemical reactions on TiO_2 may play a role on decreased pH and enhanced total Fe dissolution. Yet, the current study was unable to quantify any formation of nitrous acid in the solutions due to the low detection limits of available instrumentation. Additionally, under these experimental conditions, relatively low levels of nitrous acid could be also caused by co-adsorbed water on the mineral surface and partitioning of nitrous acid with the gas phase (Goodman et al., 1999; Su et al., 2011; Wild et al., 2016; Ostaszewski et al., 2018). From our results, we postulate that photochemical and redox-coupling reactions, at least in part, enhance the dissolution of iron in mineral dust in the presence of TiO_2 and solar flux. In addition, on a per-mass basis, the extents of total iron dissolution for the "TF3 + TiO_2" sample were more or less similar to that of the Stop 15 sample under both dark and light conditions. Thus, these results further confirm that the presence of Ti (or TiO_2) in the mineral dust mixture enhances the total iron dissolution, and consequently the bioavailable Fe to aquatic life.

Albeit the TiO_2 found in the atmosphere can be weathered and some of it perhaps amorphous, the studies done with synthesized amorphous titania suggest that these synergistic effects are preserved regardless the crystallinity of TiO_2 (Fig. S5 and Table S7).

3.2.1.2. Dissolved Fe(II) fraction. The dissolved Fe in mineral dust may become bioavailable upon deposition. Given the solubility differences between Fe(II) and Fe(III), the speciation of dissolved Fe is vital. Being more soluble, Fe(II) is likely to be more bioavailable. As previously mentioned, the Fe(II)-bearing solid phases yielded higher dissolved Fe (II) concentrations under dark conditions compared to Fe(III) phases. On the other hand, Fe(III) oxides and oxyhydroxides that yielded little or no dissolved Fe(II) under dark conditions, produced significantly higher Fe(II) via photoreductive dissolution under light conditions (Zhu et al., 1993; Rubasinghege et al., 2010). Hence, these studies on Fe(II) speciation imply its strong dependence on the source material and environmental conditions such as the availability of sunlight.

On a surface-area basis, the different samples yielded a range of dissolved Fe(II) concentrations as a function of reaction time in the presence and absence of light. The mass normalized comparison is provided in Fig. S3. The SASP and Stop15 samples have higher dissolved Fe(II) concentrations compared to the other two samples, especially under dark conditions (Fig. 5). Dissolved Fe(II) fractions (= ([Fe (II)]/[Total Fe]) × 100) after 48 h elapsed for the Stop15, BK1, SASP, and TF3 samples at pH 2 under dark were 17%, 14%, 69%, and 15%, respectively (Table 3). Under the same experimental conditions, for the "TF3 + TiO_2" sample, the dissolved Fe(II) fraction was 35% (Fig. 3(b) and Table 3); a 2.3-fold increase compared to the TF3 sample without added TiO_2. This enhancement in dissolved Fe(II) suggests the occurrence of non-photochemical redox cycling in the nitric acid solutions. TiO_2 is known to have Ti(III) surface defects (TSDs) which readily oxidize upon exposure to an oxidizing agent (Xiong et al., 2012). Perhaps TSDs play a role in reducing Fe(III) to Fe(II), thereby increasing the dissolved Fe(II) fraction. Given that the reduction potential is 0.9 V, the oxidation of Ti(III) to Ti(IV) is thermodynamically feasible (Amorello et al., 2007). Yet, whether these reaction mechanisms proceed through solid-phase with adsorbed anionic species (nitrate) or are in solution-phase is yet to be investigated. However, an analogous reaction, the reduction of nitrate by surface-bound Fe(II) or Fe(II) present in the lattice has previously been demonstrated, suggesting the possibility of a similar reaction involving the Ti(III)/Ti(IV) redox couple (Huang et al., 2016). On the other hand, there could be a counter reaction that oxidizes Fe(II) by nitrate in highly acidic solutions (Cwiertny et al., 2008). It is also important to highlight that there was no significant difference in dissolved Fe(II) fractions among the Stop15, BK1, and TF3 samples. This observation suggests that the elevated Ti levels increase dissolved Fe(II) in the solution under dark conditions; however, TiO_2 levels do not always correlate with the dissolved Fe(II) fractions. Factors other than Ti amount, such as Fe-containing minerals and clay phases, could result in high dissolved Fe(II) as indicated by the SASP sample.

Table 3
Dissolved Fe(II) fraction after 48 h of the reaction.

Sample	Dissolved Fe(II) Fraction	
	Dark	Light
Stop15	17%	7.6%
BK1	14%	n.o.
SASP	69%	36%
TF3	15%	46%
TF3 + TiO_2	35%	39%
Magnetite	33%	24%
Magnetite + TiO_2	44%	19%

n.o. – not observed.

Solar irradiation triggers photochemical reactions on surfaces of semi-conductor oxide particles yielding significant differences in daytime and nighttime chemistry. As seen in Fig. 5(c) and Table 3, natural dust TF3 showed a 3-fold enhancement in dissolved Fe(II) under light

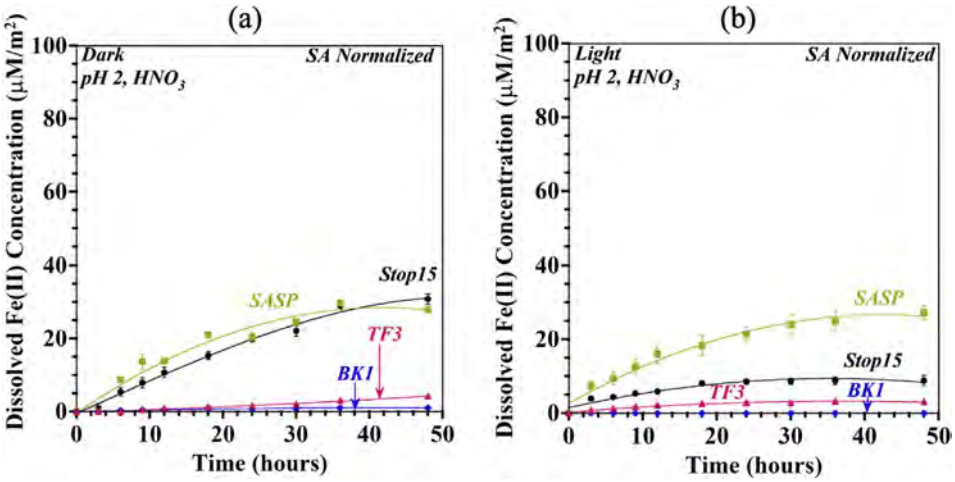

Fig. 5. The extent of dissolution of Fe(II) from the four dust samples in pH 2 nitric acid under dark and light conditions. Surface area normalized Fe(II) (a) in dark and (b) in light as a function of time. The data have been fitted to a Langmuir-type model.

conditions relative to the dark conditions. This disparity could be due to the abundant hematite in this sample, coupled with its paucity of magnetite and TiO_2, that would otherwise enhance the fraction of Fe(II) upon irradiation via photoreductive dissolution, as discussed in more detail in section 3.2.2. In contrast, the dissolved Fe(II) fractions decreased in the Stop15 (7.5%) and SASP (35.7%) samples under light conditions. The BK1 sample yielded a very low Fe(II) concentration below the detection limits. Attenuation of the dissolved Fe(II) fractions in the Stop15 and SASP samples in the presence of solar radiation may have arisen for several reasons. One such mechanism involves magnetite concentration and TiO_2 chemistry, as discussed in section 3.2.2.

Upon irradiation, the "TF3 + TiO_2" sample yeilded almost the same dissolved Fe(II) fraction as in dark conditions, in contrast to the natural TF3 sample having a ~3-fold enhancement. The fraction of dissolved Fe(II) observed for the "TF3 + TiO_2" sample was 39% under light conditions. This value is ~1.2-fold lower compared to that of just the TF3 sample under the same conditions. This result suggests a counterbalance between the enhancement of Fe(II) production due to hematite and suppression by TiO_2 in the "TF3 + TiO_2" sample. Although the elevated Ti concentration enhances the Fe(II) speciation under dark conditions in pH 2 nitric acid solutions, such concentration has a negative effect under irradiation that decreases the fraction of Fe(II) (Brown et al., 2001; Nakamura et al., 2004; Shkrob et al., 2011; Zhang et al., 2014; Silveira et al., 2017; Hettiarachchi et al., 2018a,b). The photo-generated $^{\bullet}OH$ in the presence of TiO_2, as discussed earlier, can readily oxidize Fe(II) to Fe(III), thereby reducing the overall Fe(II) production according to Eq. (1).

$$Fe(II) + {}^{\bullet}OH \rightarrow Fe(III) + OH\text{-} \quad (1)$$

Moreover, the redox coupling reactions that yielded higher dissolved Fe(II) fractions under dark conditions might have also been suppressed under light by photochemical-redox coupling reactions. These reactions, in part or in whole, might have diminished the Fe(II) production under irradiation in the Stop15 sample, because of its elevated Ti (or TiO_2) level almost equivalent to that of Fe.

3.2.2. Dissolution of iron in magnetite – a proxy for Iron(II) containing minerals

Hematite and goethite are recognized as important iron oxides in atmospheric mineral dust (Formenti et al., 2011; Maher, 2011; Reynolds et al., 2014a,b; Moskowitz et al., 2016). However, other Fe-bearing phases such as magnetite, ilmenite, as well as clay and ferromagnesian minerals are also commonly present in mineral dust (Kandler et al., 2007). These and anthropogenic bioavailable Fe sources such as coal fly ash (Chen et al., 2013) should be considered for their possible roles in atmospheric processing and Fe solubility. For an instance, Chen et al., 2012a reported Ti:Fe ratio varying from 0.2 to 0.5 in coal fly ash suggesting the presence of magnetite, TiO_2 and/or titanomagnetite (Ge et al., 2014; Devlin et al., 2016; González-Triviño et al., 2018). Having the chemical formula $FeO{\cdot}Fe_2O_3$, magnetite contains both Fe(II) and Fe(III). Further, magnetite generally has a wide band gap and is a semi-conductor oxide similar to TiO_2. Among our samples, SASP and BK1 contain relatively high magnetite amounts (~3.5% of total Fe) compared to TF3 and Stop 15 (< 1% of total Fe).

We compared total iron dissolution and Fe(II) speciation as a function of time in the magnetite sample and a "magnetite + TiO_2" sample under both dark and light conditions (Fig. 6). For the latter sample, 9 mg of magnetite were mixed with 11 mg of TiO_2 to obtain a final mass of 20 mg with Ti:Fe ratio closer to 0.98 as found in the Stop15 sample. The magnetite + TiO_2 sample showed about 1.6- and 2.1-fold enhancement of total iron dissolution under dark and light conditions, respectively, compared to the sample of pure magnetite (Fig. 6(a) and (b)). The pseudo first-order rates of total iron dissolution in the magnetite and "magnetite + TiO_2" under dark conditions were $82 \pm 4\,\mu M\,g^{-1}\,hr^{-1}$ and $241 \pm 2\,\mu M\,g^{-1}\,hr^{-1}$, respectively. Those under light conditions were $246 \pm 5\,\mu M\,g^{-1}\,hr^{-1}$ and $551 \pm 3\,\mu M\,g^{-1}\,hr^{-1}$ for the magnetite and "magnetite + TiO_2," respectively. These enhancements, along with results for the "TF3 + TiO_2" sample, exhibit the influence of TiO_2 to amplify the total Fe dissolution in mineral dust. Similar enhancements were seen with hematite and hematite + TiO_2 in our previous work (Hettiarachchi et al., 2018b). The decreasing pH of the reaction medium was observed in the magnetite + TiO_2 sample similar to that in the sample TF3 (Fig. S4). In aqueous solutions, however, magnetite may also be capable of attracting dissolved Fe ions, particularly Fe(II), yielding surface bound Fe (II); in this way, the amount of dissolved Fe in the solution will be diminished (Huang et al., 2016).

As expected, total iron dissolution of magnetite increased upon irradiation. Similar to hematite and goethite, this effect can be related to the photo-enhanced reductive dissolution where Fe(III) in magnetite is reduced and subsequently detached into the solution. Furthermore, rapid electron exchange could occur upon irradiation between Fe(II) and Fe(III), in the octahedral sites, further weakening the surface Fe-O bonds and accelerating its breakaway from the bulk magnetite structure (Huang et al., 2017). In addition, having ~2.9 eV band gap, the magnetite sample exhibited the possibility of generating hydroxyl radicals from surface-adsorbed water under irradiation that may introduce more photochemical reaction pathways. Similar to sample "TF3 + TiO_2," the magnetite sample also showed a higher total iron dissolution in the presence of TiO_2 and solar flux compared to the sample of pure magnetite under the same conditions. We attribute these results to photochemical reactions involving TiO_2 as discussed earlier in section 3.2.1. However, in natural dusts, these photochemical and chemical reactions always balance and counterbalance to obtain overall iron dissolution.

In the absence of solar radiation, the dissolved Fe(II) fraction from magnetite was 33% of the total Fe. Given the fact that magnetite contains a Fe(II):Fe(III) ratio of 1:2, these results are in good agreement with the Fe(II) content depicted by the chemical formula. These data further suggest that no particular redox cycling is taking place under these conditions. The dissolved Fe(II) fraction in the "magnetite + TiO_2" sample was 44% under dark conditions highlighting a 1.3-fold increase compared to that of the pure magnetite sample under the same conditions. Unlike hematite and goethite, the dissolved Fe(II) fraction in magnetite decreases to 24% upon irradiation suggesting photo-induced redox coupling reactions. The magnetite + TiO_2 showed an even lesser amount (19%) of dissolved Fe (II) in the presence of light. This result represents a 2.3-fold decrease compared to its dark counterpart and a 1.3-fold decrease compared to the sample of just magnetite under light. Under irradiation and in the presence of adsorbed anions such as oxalate, magnetite has produced radical species, including $^{\bullet}OH$ (Huang et al., 2017). Besides, some adsorbed anionic species such as nitrate can act as chromophores, thereby initiating photochemical reactions upon photo-excitation (Schuttlefield et al., 2008). Such phenomena and our findings suggest the possibility of photochemical oxidation of dissolved Fe(II) by radical species, generated under irradiation. Therefore, the suppression of dissolved Fe(II) production in SASP and possibly in BK1 upon irradiation may have been influenced by their magnetite content, rather than lower Ti levels. Given that magnetite is not the major iron oxide component in mineral dust, its minimum concentration to counteract hematite and/or goethite needs to be evaluated. For example, the suppression of dissolved Fe(II) in the Stop15 sample under light conditions may be attributed to its higher Ti concentration rather than its relatively low magnetite. This argument is further supported by the result that dissolved Fe(II) fractions in the TF3 sample, having low magnetite (0.8% of Total Fe) and Ti concentrations, increased rather than decreased under the irradiation.

4. Conclusions

The current study reveals several important influences of

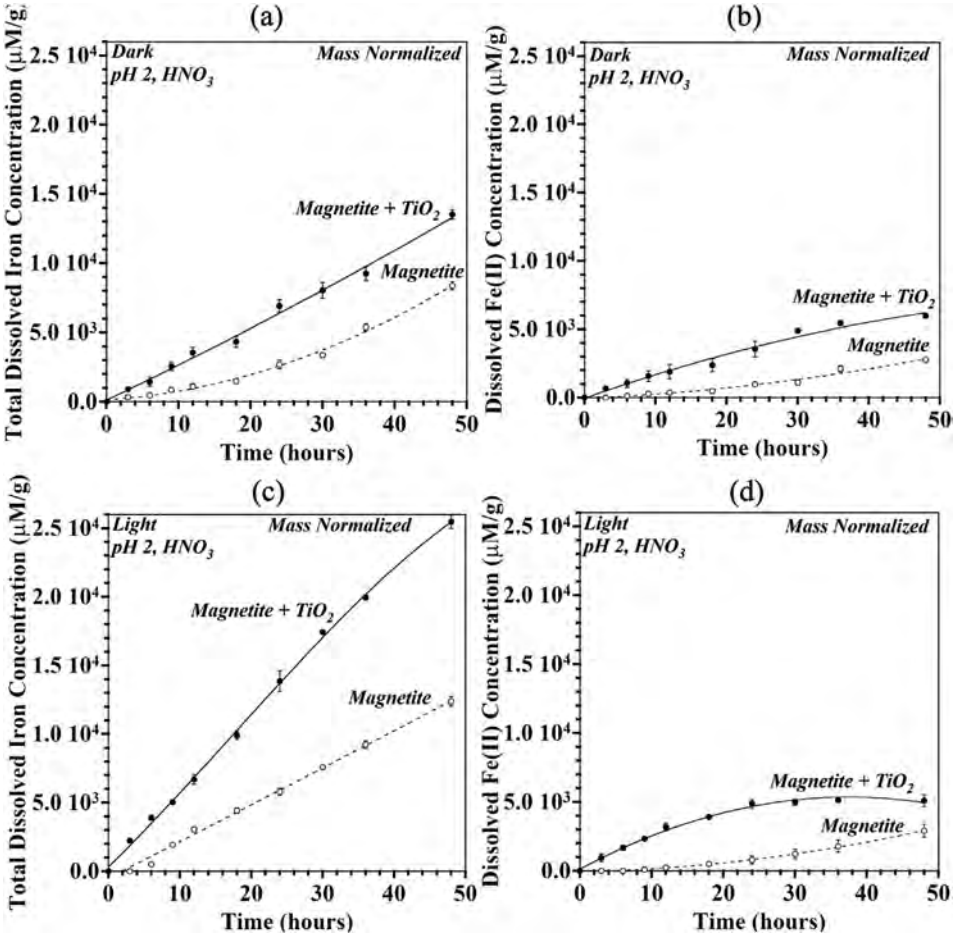

Fig. 6. A mass normalized comparison of the dissolution of total iron and Fe(II) as a function of time from pure magnetite and magnetite with added TiO_2 (anatase). (a) Total iron in dark (b) Fe(II) concentration in dark (c) total iron in light (d) Fe(II) concentration in light. The data have been fitted to a Langmuir-type model.

mineralogy and chemical composition on iron dissolution and Fe(II) speciation in mineral dust aerosols under atmospherically relevant conditions using four natural dust samples and a pure magnetite sample. Total iron dissolution did not always correlate with Fe contents or particle properties of the samples. Total iron dissolution also heavily depended on the types of Fe-bearing minerals and on the presence of non-Fe-containing minerals. Regardless of the amount of total Fe in the mineral dust, elevated levels of Ti (usually as TiO_2, regardless of its crystallinity) yielded significantly higher amounts of total dissolved iron under both dark and light conditions. These data further indicate a strong correlation between total dissolved Fe and Ti:Fe ratio. These effects can be clearly seen in natural dust samples having elevated Ti levels as well as in samples of dust and pure magnetite that were artificially enriched in TiO_2. Under dark conditions, apparently this enhancement was influenced, in part or in whole, by the decrease of solution pH in the presence of TiO_2. Under the light conditions, total iron dissolution was further enhanced by additional photochemical reaction pathways. Such pathways are initiated by hydroxyl radicals that are generated from surface-adsorbed water on the TiO_2 surface. Nevertheless, elevated levels of Ti in mineral dust resulted in higher dissolved Fe(II) fractions under dark conditions, whereas it was suppressed upon irradiation. In the absence of light, redox coupling reactions apparently occur among titanium surface defects (TSDs), Ti(III) sites on the TiO_2 surface, and Fe(III) in the medium to produce more Fe (II) in the solution. Under solar radiation, photo-generated hydroxyl radicals oxidize Fe(II) to Fe(III), thereby diminishing the dissolved Fe (II) fraction.

This work also evaluated Fe dissolution from magnetite, which is commonly found in dusts along with ferric oxide minerals. Natural dust samples with relatively elevated levels of magnetite showed enhanced total iron dissolution upon irradiation. This finding may be attributed to the photoreductive dissolution triggered by electron exchange between Fe(II) and Fe(III) in octahedral sites of the magnetite bulk structure. In contrast to hematite and goethite, magnetite suppresses dissolved Fe(II) production upon irradiation, suggesting radical mediated photo-oxidation of Fe(II) to Fe(III). Furthermore, magnetite with added TiO_2 demonstrates behavioral trends similar to those in Ti-bearing natural dusts.

Our results for magnetite have several implications for dust-iron dissolution and the subsequent delivery of bioavailable iron to oceans and lakes. First, magnetite is intimately associated with titanium in many rock types and thus in the sediments and soils derived from them. Titanium is found in solid-solution series minerals between pure magnetite and ulvöspinel ($TiFe_2^{2+}O_4$). Common high-temperature oxidation of such minerals, for example, in extrusive rocks upon initial cooling, produces ilmenite within magnetite. Further oxidation can lead to the production of anatase or rutile within magnetite grains and on grain margins. Many other titaniferous minerals such as those in the pseudobrookite solid-solution series, $(Fe^{3+},Fe^{2+})_2(Ti,Fe^{2+})O_5$, are found in these associations (Haggerty, 1976; Lindsley, 1991). Thus, magnetite usually carries with itself Ti in ways that may enhance its solubility. Second, magnetite may be considered a proxy for other ferrous iron minerals because it occurs commonly with minerals such as hornblendes, pyroxenes, and olivines in many rock types (Lindsley, 1991; Reynolds et al., 2014b). The potential for these other minerals to yield soluble Fe is worthy of future study. Finally, magnetite is a common by-

product of fossil-fuel combustion in industrial, extraction, smelting, and transportation activities. In such occurrences, magnetite may not be associated with Ti, but it can be with other metal oxides such as copper (Reynolds et al., 2010).

Each of our samples represents documented or inferred environmental effects of atmospherically transported dust. With respect to sample BK1 from southern Africa, recent interest in dust emission and transport from the Namib and Kalahari deserts focuses on Fe supply to the South Atlantic Ocean (Bhattacchan et al., 2012; Dansie et al., 2017, 2018; Vainer et al., 2018). Chemical characterization studies have shown some source sediments to contain TiO_2, and its presence might contribute to the reported high Fe solubility in these dusts. The current study uses samples TF3 and Stop15 to represent clastic dusts, differing in Fe oxide mineralogy, from the southern Colorado Plateau that are typically transported several hundred kilometers to and across the central Rocky Mountains (Neff et al., 2013; Reynolds et al., 2016). Such dust falls during winter and spring, represented by sample SASP, decrease snow-cover albedo to accelerate late spring melting (Painter et al., 2012; Skiles et al., 2015). Dust deposited onto snow or directly onto the ground is incorporated into soil and can be washed into freshwater montane lakes adding nutrients to these environments (Lawrence et al., 2010, 2013; Zhang et al., 2017). Understanding the bioavailable Fe content for freshwater aquatic life is important for understanding the microbial community composition. Through this understanding, it may be possible to control the blooming of toxic cyanobacteria in these lakes (Xing et al., 2011; Paerl, 2017).

Current biogeochemical models use total Fe, just hematite, or just ferric oxide (hematite plus goethite), contents to estimate the bioavailable iron portion in mineral dusts for simulating effects of ocean fertilization on the carbon cycle. For instance, these atmospheric models for iron deposition usually assume an average value of 3.5 wt% as the total Fe content in mineral dusts, (Lohmann et al., 2007; Mahowald et al., 2009; Ito et al., 2014; Myriokefalitakis et al., 2018). However, the chemical compositions of these dusts are highly variable, and the Fe mineralogy is more complex than currently considered. We find that non-Fe-containing minerals such as TiO_2 can greatly enhance the total Fe dissolution regardless of the Fe concentrations in the mineral dust. Including these synergistic effects among metals could improve the projection of iron flux to surface waters. In addition, further experiments are suggested here to better understand the complex mechanisms of metal-metal synergistic and antagonistic effects, so that this information could be incorporated into such atmospheric models to obtain more reliable simulations of the Earth's biogeochemical cycles.

Declaration of interests

The authors declare that they have no known competing financial interests or personal relationships that could have appeared to influence the work reported in this paper.

Acknowledgments

This research did not receive any specific grant from funding agencies in the public, commercial, or not-for-profit sectors. The authors thank the Department of Chemistry, New Mexico Institute of Mining and Technology. The Institute for Rock Magnetism (IRM) is supported by the Instruments and Facilities Program of the NSF Division of Earth Science. This is IRM contribution 1803.

The authors are grateful to Paolo D'Odorico and Abi Bhattachan for providing the Kalahari sample, to Ray Kokaly for determining mineralogy from reflectance spectroscopy, and to Gary Skipp for determining mineralogy from X-ray diffraction. This research was supported in part by the Climate and Land Use Change Program of the U.S. Geological Survey. Any use of trade, product, or firm names is for descriptive purposes only and does not imply endorsement by the U.S. Government. The authors also thank Richard Wanty for his thorough and insightful review which greatly improved this manuscript. All the raw data measurements that we used to plot the graphs illustrated in the figures and provided in tables are in the Supplemental Material.

Appendix A. Supplementary data

Supplementary data to this article can be found online at https://doi.org/10.1016/j.atmosenv.2019.02.037.

References

Amorello, D., Gambino, V., Romano, V., Zingales, R., 2007. The formal redox potential of the Ti(IV, III) couple at 25 °C in 1 M HCl 2 M NaCl medium. Ann. Chim. 97 (8), 713–721. https://doi.org/10.1002/adic.200790055.

Bard, A.J., Parsons, R., Jordan, J., 1985. Standard Potentials in Aqueous Solutions. Marcel Dekker, Basel, New York, pp. 391–413.

Bhattachan, A., Dodorico, P., Baddock, M.C., Zobeck, T.M., Okin, G.S., Cassar, N., 2012. The southern Kalahari: a potential New dust source in the southern hemisphere? Environ. Res. Lett. 7, 1–7. https://doi.org/10.1088/1748-9326/7/2/024001.

Bhattachan, A., Reche, I., D'Odorico, P., 2016. Soluble ferrous iron (Fe (II)) enrichment in airborne dust. J. Geophys. Res. 121, 10153–10160. https://doi.org/10.1002/2016JD025025.

Biswakarma, J., Kang, K., Borowski, S.C., Schenkeveld, W.D.C., Kraemer, S.M., Hering, J.G., Hug, S.J., 2019. Fe(II)-Catalyzed ligand-controlled dissolution of iron(hydr) oxides. Environ. Sci. Technol. 53, 44. https://doi.org/10.1021/acs.est.8b03910.

Borgatta, J., Paskavitz, A., Kim, D., Navea, J.G., 2016. Comparative evaluation of iron leach from different sources of fly ash under atmospherically relevant conditions. Environ. Chem. 13, 902–912. https://doi.org/10.1071/EN16046.

Brand, R.A., 1987. Improving the validity of hyperfine field distributions from metallic alloys. Part I: unpolarized source. Nucl. Instrum. Methods Phys. Res. B. 28, 398–405.

Briggs, P.H., 2002. The determination of forty elements in geological and botanical samples by inductively coupled plasma-atomic emission spectrometry. In: Taggart Jr.J.E. (Ed.), Analytical Methods for Chemical Analysis of Geologic and Other Materials. U.S. Geological Survey Open-File Report 02–223, pp. I1–I14.

Brown, S.S., Burkholder, J.B., Talukdar, R.K., Ravishankara, A.R., 2001. Reaction of hydroxyl radical with nitric acid: insights into its mechanism. J. Phys. Chem. 105, 1605–1614. https://doi.org/10.1021/jp002394m.

Carter-Stiglitz, B., Moskowitz, B., Solheid, P., Berquó, T.S., Jackson, M., Kosterov, A., 2006. Low-temperature magnetic behavior of multidomain titanomagnetites: TM0, TM16, and TM35. J. Geophys. Res. 111, B12S05. https://doi.org/10.1029/2006JB004561.

Chen, H., Grassian, V.H., 2013. Iron dissolution of dust source materials during simulated acidic processing: the effect of sulfuric, acetic, and oxalic acids. Environ. Sci. Technol. 47, 10312–10321. https://doi.org/10.1021/es401285s.

Chen, H., Laskin, A., Baltrusaitis, J., Gorski, C.A., Scherer, M.M., Grassian, V.H., 2012a. Coal fly ash as a source of iron in atmospheric dust. Environ. Sci. Technol. 46, 2112–2120. https://doi.org/10.1021/es204102f.

Chen, H., Nanayakkara, C.E., Grassian, V.H., 2012b. Titanium dioxide photocatalysis in atmospheric chemistry. Chem. Rev. 112, 5919–5948. https://doi.org/10.1021/cr3002092.

Clark, R.N., Swayze, G.A., Wise, R.A., Live, K.E., Hoefen, T.M., Kokaly, R.F., Sutley, S.J., 2007. USGS Digital Spectral Library Splib06a. U.S. Geological Survey Data Series 231.

Cwiertny, D.M., Baltrusaitis, J., Hunter, G.J., Laskin, A., Scherer, M.M., Grassian, V.H., 2008. Characterization and acid-mobilization study of iron-containing mineral dust source materials. J. Geophys. Res. Atmos. 113, 1–18. https://doi.org/10.1029/2007JD009332.

D'Souza, L.P., Shree, S., Balakrishna, G.R., 2013. Bifunctional titania float for metal ion reduction and organics degradation, via sunlight. Ind. Eng. Chem. Res. 52, 16162–16168. https://doi.org/10.1021/ie402592k.

Dansie, A.P., Thomas, D.S.G., Wiggs, G.F.S., Munkittrick, K.R., 2018. Spatial variability of ocean fertilizing nutrients in the dust-emitting ephemeral river catchments of Namibia. Earth Surf. Process. Landforms 43, 563–578. https://doi.org/10.1002/esp.4207.

Dansie, A.P., Wiggs, G.F.S., Thomas, D.S.G., Washington, R., 2017. Measurements of windblown dust characteristics and ocean fertilization potential: the ephemeral river valleys of Namibia. Aeolian Research 29, 30–41. https://doi.org/10.1016/j.aeolia.2017.08.002.

De Jong, J., Schoemann, V., Lannuzel, D., Croot, P., De Baar, H., Tison, J.-L., 2012. Natural iron fertilization of the atlantic sector of the Southern Ocean by continental shelf sources of the antarctic Peninsula. J. Geophys. Res. 117. https://doi.org/10.1029/2011JG001679.

Desboeufs, K.V., Losno, R., Colin, J.L., 2003. Relationship between droplet pH and aerosol dissolution kinetics: effects of incorporated aerosol particles on droplet pH during cloud processing. J. Atmos. Chem. 46, 159–172. https://doi.org/10.1023/A:1026011408748.

Devlin, E., Bourliva, A., Papadopoulou, L., Aidona, E., Sanakis, Y., Simeonidis, K., Vourlias, G., 2016. Enrichment and oral bioaccessibility of selected trace elements in fly ash-derived magnetic components. Environ. Sci. Pollut. Res. 24, 2337–2349. https://doi.org/10.1007/s11356-016-7967-4.

Doney, S.C., Lima, I., Lindsay, K., Moore, J.K., Dutkiewicz, S., Friedrichs, M.A.M., Matear, R.J., 2001. Marine biogeochemical modeling: recent advances and future challenges.

Oceanography 4, 93–107.
El Ghandoor, H., Zidan, H.M., Khalil, M.M.H., Ismail, M.I.M., 2012. Synthesis and some physical properties of magnetite (Fe_3O_4) nanoparticles. Int. J. Electrochem. Sci. 7, 5734–5745. https://doi.org/10.1080/01418638008221885.
Erdner, D.L., Anderson, D.M., 1999. Ferredoxin and flavodoxin as biochemical indicators of iron limitation during open-ocean iron enrichment. Limnol. Oceanogr. 44, 1609–1615. https://doi.org/10.4319/lo.1999.44.7.1609.
Formenti, P., Schütz, L., Balkanski, Y., Desboeufs, K., Ebert, M., Kandler, K., Petzold, A., Scheuvens, D., Weinbruch, S., Zhang, D., 2011. Recent progress in understanding physical and chemical properties of african and asian mineral dust. Atmos. Chem. Phys. 11, 8231–8256. https://doi.org/10.5194/acp-11-8231-2011.
Formenti, P., Elbert, W., Maenhaut, W., Haywood, J., Andreae, M.O., 2003. Chemical composition of mineral dust aerosol during the Saharan dust experiment (SHADE) airborne campaign in the Cape Verde region, September 2000. J. Geophys. Res. 108, 3. http://doi.org/10.1029/2002jd002648.
Frogner, P., Reynir Gíslason, Sigurdur, Óskarsson, Niels, 2001. Fertilizing potential of volcanic ash in ocean surface water. Geology 29 (6), 487 487. http://10.1130/0091-7613(2001)029 < 0487:FPOVAI > 2.0.CO;2.
Fu, H., Cwiertny, D.M., Carmichael, G.R., Scherer, M.M., Grassian, V.H., 2010. Photoreductive dissolution of Fe-containing mineral dust particles in acidic media. J. Geophys. Res. Atmos. 115, 1–12. https://doi.org/10.1029/2009JD012702.
Gankanda, A., Grassian, V.H., 2014. Nitrate photochemistry on laboratory proxies of mineral dust aerosol: wavelength dependence and action spectra. J. Phys. Chem. C 118, 29117–29125. https://doi.org/10.1021/jp504399a.
Ge, L.Q., Tang, J.H., Yao, Z.T., Ji, X.S., Sarker, P.K., Xia, M.S., Xi, Y.Q., 2014. A comprehensive review on the applications of coal fly ash. Earth Sci. Rev. 141, 105–121. https://doi.org/10.1016/j.earscirev.2014.11.016.
González-Triviño, I., Benítez-Guerrero, M., Carda Castelló, J., Moreno, B., Pascual-Cosp, J., 2018. Synthesis and characterization of ferrimagnetic glass-ceramic frit from waste. Int. J. Appl. Ceram. Technol. 15, 775–782. https://doi.org/10.1111/ijac.12850.
Goodman, A.L., Bernard, E.T., Grassian, V.H., 2001. Spectroscopic study of nitric acid and water adsorption on oxide particles: enhanced nitric acid uptake kinetics in the presence of adsorbed water. J. Phys. Chem. 105, 6443–6457. https://doi.org/10.1021/jp003722l.
Goodman, A.L., Underwood, G.M., Grassian, V.H., 1999. Heterogeneous reaction of NO_2: characterization of gas-phase and adsorbed products from the reaction, $2NO_{2(g)} + H_2O_{(a)} \rightarrow HONO_{(g)} + HNO_{3(a)}$ on hydrated silica particles. J. Phys. Chem. 103, 7217–7223. https://doi.org/10.1021/jp9910688.
Grybos, M., Michot, L.J., Skiba, M., Billard, P., Mustin, C., 2010. Dissolution of anisotropic colloidal mineral particles: evidence for basal surface reactivity of nontronite. J. Colloid Interface Sci. 343, 433–438. https://doi.org/10.1016/j.jcis.2009.11.058.
Haggerty, S.E., 1976. Oxidation of opaque mineral oxides in basalts. In: In: Rumble, D. (Ed.), Oxide Minerals: Mineralogical Society of America Short Course Notes, vol. 3 chap. 4, p. Hg-1-Hg-100.
Held, I.M., 2005. The gap between simulation and understanding in climate modeling. Bull. Am. Meteorol. Soc. 1609–1614. November. https://doi.org/10.1175/BAMS-86-11-1609.
Henderson, M.A., 2003. Surface stabilization of organics on hematite by conversion from terminal to bridging adsorption structures. Geochem. Cosmochim. Acta 67, 1055–1063.
Henderson, M.A., 2011. Surface chemistry of trimethyl phosphate on α-Fe_2O_3. J. Phys. Chem. C 115, 23527–23534. https://doi.org/10.1021/jp208978d.
Hettiarachchi, E., Hurab, O., Rubasinghege, G., 2018a. Atmospheric processing and iron mobilization of ilmenite: iron-containing ternary oxide in mineral dust aerosol. J. Phys. Chem. 122, 1291–1302. https://doi.org/10.1021/acs.jpca.7b11320.
Hettiarachchi, E., Reynolds, R.L., Goldstein, H.L., Moskowitz, B., Rubasinghege, G., 2018b. Iron dissolution and speciation in atmospheric mineral dust: metal-metal synergistic and antagonistic effects. Atmos. Chem. Phys. 187, 417–423. https://doi.org/10.1016/j.atmosenv.2018.06.010.
Huang, M., Zhou, T., Wu, X., Mao, J., 2017. Distinguishing homogeneous-heterogeneous degradation of norfloxacin in a photochemical fenton-like system (Fe_3O_4/UV/oxalate) and the interfacial reaction mechanism. Water Res. 119, 47–56. https://doi.org/10.1016/j.watres.2017.03.008.
Huang, Y.H., Asce, M., Zhang, T.C., Asce, F., 2016. Nitrate reduction by surface-bound Fe (II) on solid surfaces at near-neutral pH and ambient temperature. J. Environ. Eng. 14, 1–7. https://doi.org/10.1061/(ASCE)EE.1943-7870.
Ingall, E.D., Feng, Y., Longo, A.F., Lai, B., Shelley, R.U., Landing, W.M., Morton, P.L., Nenes, A., Mihalopoulos, N., Violaki, K., Gao, Y., Sahai, S., Castorina, E., 2018. Enhanced iron solubility at low pH in global aerosols. Atmosphere 9, 1–17. https://doi.org/10.3390/atmos9050201.
Ito, A., Lin, G., Penner, J.E., 2018. Radiative forcing by light-absorbing aerosols of pyrogenetic iron oxides. Sci. Rep. 8, 1–11. https://doi.org/10.1038/s41598-018-25756-3.
Ito, A., Xu, L., 2014. Response of acid mobilization of iron-containing mineral dust to improvement of air quality projected in the future. Atmos. Chem. Phys. 14, 3441–3459. https://doi.org/10.5194/acp-14-3441-2014.
Jackson, G.A., Burd, A.B., 2015. Simulating aggregate dynamics in ocean biogeochemical models. Prog. Oceanogr. 133, 55–65. https://doi.org/10.1016/j.pocean.2014.08.014.
Journet, E., Desboeufs, K.V., Caquineau, S., Colin, J.L., 2008. Mineralogy as a critical factor of dust iron solubility. Geophys. Res. Lett. 35, 1–5. https://doi.org/10.1029/2007GL031589.
Kandler, K., Benker, N., Bundke, U., Cuevas, E., Ebert, M., Knippertz, P., Rodríguez, S., Schütz, L., Weinbruch, S., 2007. Chemical composition and complex refractive index of Saharan mineral dust at Izaña, tenerife (Spain) derived by electron microscopy. Atmos. Environ. 41, 8058–8074. https://doi.org/10.1016/j.atmosenv.2007.06.047.
Kang, K., Schenkeveld, W.D.C., Biswakarma, J., Borowski, S.C., Hug, S.J., Hering, J.G., Kraemer, S.M., 2019. Low Fe(II) concentrations catalyze the dissolution of various Fe (III) (hydr)oxide minerals in the presence of diverse ligands and over a broad pH range. Environ. Sci. Technol. 53, 98–107. https://doi.org/10.1021/acs.est.8b03909.
Krueger, B.J., Grassian, V.H., Cowin, J.P., Laskin, A., 2004. Heterogeneous chemistry of individual mineral dust particles from different dust source regions: the importance of particle mineralogy. Atmos. Environ. 38, 6253–6261. https://doi.org/10.1016/j.atmosenv.2004.07.010.
Lawrence, C.R., Reynolds, R.L., Ketterer, M., Neff, J.C., 2013. Aeolian controls on soil geochemistry and weathering fluxes in high-elevation ecosystems of the Rocky mountains. USA: Geochem. Cosmochim. Acta 107, 27–46.
Lawrence, C.R., Painter, T.H., Landry, C., Neff, J.C., 2010. The contemporary composition of aeolian dust deposited in the san juan mountains, Colorado, USA. J. Geophys. Res. 115. http://doi.org/10.1029/2009JG001077.
Lesko, D.M.B., Coddens, E.M., Swomley, H.D., Welch, R.M., Borgatta, J., Navea, J.G., 2015. Photochemistry of nitrate chemisorbed on various metal oxide surfaces. Phys. Chem. Chem. Phys. 17, 20775–20785. https://doi.org/10.1039/c5cp02903a.
Li, W., Xu, L., Liu, X., Zhang, J., Lin, Y., Yao, X., Gao, H., Zhang, D., Chen, J., Wang, W., Harrison, R.M., Zhang, X., Shao, L., Fu, P., Nenes, A., Shi, Z., 2017. Air pollution–aerosol interactions produce more bioavailable iron for ocean ecosystems. Sci. Adv. 3, 1–6. https://doi.org/10.1126/sciadv.1601749.
Oxide minerals: petrologic and magnetic significance. Lindsley, D.H. (Ed.), Reviews in Mineralogy 25, 509 Mineralogical Society of America.
Lohmann, U., Quaas, J., Kinne, S., Feichter, J., 2007. Different approaches for constraining global climate models of the anthropogenic indirect aerosol effect. Bull. Am. Meteorol. Soc. February 243–249. https://doi.org/10.1175/BAMS-88-2-243.
Lu, W., Zhao, W., Balsam, W., Lu, H., Liu, P., Lu, Z., Ji, J., 2017. Iron mineralogy and speciation in clay-sized fractions of Chinese desert sediments. J. Geophys. Res. Atmos. 122, 13458–13471. https://doi.org/10.1002/2017JD027733.
Maher, B.A., 2011. The magnetic properties of quaternary aeolian dusts and sediments, and their palaeoclimatic significance. Aeolian Research 3, 87–144. http://doi:10.1016/j.aeolia.2011.01.005.
Mahowald, N.M., Baker, A.R., Bergametti, G., Brooks, N., Duce, R.A., Jickells, T.D., Kubilay, N., Prospero, J.M., Tegen, I., 2005. Atmospheric global dust cycle and iron inputs to the ocean. Glob. Biogeochem. Cycles 19, 1–17. https://doi.org/10.1029/2004GB002402.
Mahowald, N.M., Engelstaedter, S., Luo, C., Sealy, A., Artaxo, P., Benitez-Nelson, C., Bonnet, S., Chen, Y., Chuang, P.Y., Cohen, D.D., Dulac, F., Herut, B., Johansen, A.M., Kubilay, N., Losno, R., Maenhaut, W., Paytan, A., Prospero, J.M., Shank, L.M., Siefert, R.L., 2009. Atmospheric iron deposition: global distribution, variability, and human perturbations. Ann. Rev. Mar. Sci. 1, 245–278. https://doi.org/10.1146/annurev.marine.010908.163727.
Martin, J.H., 1990. Glacial-interglacial CO_2 Change: the iron hypothesis. Paleoceanography 5 (1), 1–13. http://doi.org/10.1029/PA005i001p00001.
Meskhidze, N., Chameides, W.L., Nenes, A., 2005. Dust and pollution: a recipe for enhanced ocean fertilization? J. Geophys. Res. Atmos. 110, 1–23. https://doi.org/10.1029/2004JD005082.
Moskowitz, B.M., Reynolds, R.L., Goldstein, H.L., Berquó, T.S., Kokaly, R.F., Bristow, C.S., 2016. Iron oxide minerals in dust-source sediments from the bodélé depression, Chad: implications for radiative properties and Fe bioavailability of dust plumes from the Sahara. Aeolian Res. 22, 93–106. https://doi.org/10.1016/j.aeolia.2016.07.001.
Moteki, N., Adachi, K., Ohata, S., Yoshida, A., Harigaya, T., Koike, M., Kondo, Y., 2017. Anthropogenic iron oxide aerosols enhance atmospheric heating. Nat. Commun. 8, 1–11. https://doi.org/10.1038/ncomms15329.
Myriokefalitakis, S., Ito, A., Kanakidou, M., Nenes, A., Krol, M.C., Mahowald, N.M., Scanza, R.A., Hamilton, D.S., Johnson, M.S., Meskhidze, N., Kok, J.F., Guieu, C., Baker, A.R., Jickells, T.D., Sarin, M.M., Bikkina, S., Shelley, R., Bowie, A., Perron, M.M.G., Duce, R.A., 2018. Reviews and syntheses: the GESAMP atmospheric iron deposition model intercomparison study. Biogeosciences 15, 6659–6684. https://doi.org/10.5194/bg-15-6659-2018.
Nakamura, R., Nakato, Y., 2004. Primary intermediates of oxygen photoevolution reaction on TiO_2 (rutile) particles, revealed by in situ FTIR absorption and photoluminescence measurements. J. Am. Chem. Soc. 126, 1290–1298. https://doi.org/10.1021/ja0388764.
Neff, J.C., Reynolds, R.L., Munson, S.M., Fernandez, D., Belnap, J., 2013. The role of dust storms in total atmospheric particle concentrations at two sites in the Western U.S. J. Geophys. Res. Atmos. 118, 11201–11212. https://doi.org/10.1002/jgrd.50855.
Nenes, A., Krom, M.D., Mihalopoulos, N., Van Cappellen, P., Shi, Z., Bougiatioti, A., Zarmpas, P., Herut, B., 2011. Atmospheric acidification of mineral aerosols: a source of bioavailable phosphorus for the oceans. Atmos. Chem. Phys. 11, 6265–6272. https://doi.org/10.5194/acp-11-6265-2011.
Ohata, S., Yoshida, A., Moteki, N., Adachi, K., Takahashi, Y., Kurisu, M., Koike, M., 2018. Abundance of light-absorbing anthropogenic iron oxide aerosols in the urban atmosphere and their emission sources. J. Geophys. Res. Atmos. 123, 8115–8134. https://doi.org/10.1029/2018JD028363.
Ostaszewski, C.J., Stuart, N.M., Lesko, D.M.B., Kim, D., Lueckheide, M.J., Navea, J.G., 2018. Effects of coadsorbed water on the heterogeneous photochemistry of nitrates adsorbed on TiO_2. J. Phys. Chem. 122, 6360–6371. https://doi.org/10.1021/acs.jpca.8b04979.
Pabortsava, K., Lampitt, R.S., Benson, J., Crowe, C., McLachlan, R., Le Moigne, F.A.C., Mark Moore, C., Pebody, C., Provost, P., Rees, A.P., Tilstone, G.H., Woodward, E.M.S., 2017. Carbon sequestration in the deep atlantic enhanced by Saharan dust. Nat. Geosci. 10, 189–196. https://doi.org/10.1038/ngeo2899.
Paerl, H.W., 2017. Controlling cyanobacterial harmful blooms in freshwater ecosystems. Microb. Biotechnol. 10, 1106–1110. https://doi.org/10.1111/1751-7915.12725.

Painter, T.H., Skiles, S.M.K., Deems, J.S., Bryant, A.C., Landry, C.C., 2012. Dust radiative forcing in snow of the upper Colorado river basin: Part 1. A 6-year record of energy balance, radiation, and dust concentrations. Water Resour. Res. 48, 1–14. https://doi.org/10.1029/2012WR011985.

Paris, R., Desboeufs, K.V., Journet, E., 2011. Variability of dust iron solubility in atmospheric waters: investigation of the role of oxalate organic complexation. Atmos. Environ. 45, 6510–6517. https://doi.org/10.1016/j.atmosenv.2011.08.068.

Podczeck, F., 1997. A shape factor to assess the shape of particles using image analysis. Powder Technol. 93, 47–53.

Poulton, S.W., Canfield, D.E., 2005. Development of a sequential extraction procedure for iron: implications for iron partitioning in continentally derived particulates. Chem. Geol. 214, 209–221. https://doi.org/10.1016/j.chemgeo.2004.09.003.

Reynolds, R.L., Cattle, S.R., Moskowitz, B.M., Goldstein, H.L., Yauk, K., Flagg, C.B., Berquó, T.S., Kokaly, R.F., Morman, S., Breit, G.N., 2014a. Iron oxide minerals in dust of the red dawn event in eastern Australia, September 2009. Aeolian Res 15, 1–13. https://doi.org/10.1016/j.aeolia.2014.02.003.

Reynolds, R.L., Goldstein, H.L., Moskowitz, B.M., Bryant, A.C., Skiles, S.M.K., Kokaly, R.F., Flagg, C.B., Yauk, K., Berquó, T., Breit, G., Ketterer, M., Fernandez, D., Miller, M.E., Painter, T.H., 2014b. Composition of dust deposited to snow cover in the Wasatch range (Utah, USA): controls on radiative properties of snow cover and comparison to some dust-source sediments. Aeolian Res 15, 73–90. https://doi.org/10.1016/j.aeolia.2013.08.001.

Reynolds, R.L., Mordecai, J.S., Rosenbaum, J.G., Ketterer, M.E., Walsh, M.K., Moser, K.A., 2010. Compositional changes in sediments of Subalpine lakes, uinta mountains, Utah: evidence for the effects of human activity on atmospheric dust inputs. J. Paleolimnol. 161–175. https://doi.org/10.1007/s10933-009-9394-8.

Reynolds, R.L., Munson, S.M., Fernandez, D., Goldstein, H.L., Neff, J.C., 2016. Concentrations of mineral aerosol from desert to plains across the central Rocky mountains, Western United States. Aeolian Res 23, 21–35. https://doi.org/10.1016/j.aeolia.2016.09.001.

Rubasinghege, G., Lentz, R.W., Scherer, M.M., Grassian, V.H., 2010. Simulated atmospheric processing of iron oxyhydroxide minerals at low pH: roles of particle size and acid anion in iron dissolution. Proc. Natl. Acad. Sci. Unit. States Am. 107, 6628–6633. https://doi.org/10.1073/pnas.0910809107.

Schuttlefield, J., Rubasinghege, G., El-Maazawi, M., Bone, J., Grassian, V.H., 2008. Photochemistry of adsorbed nitrate. J. Am. Chem. Soc. 130, 12210–12211. https://doi.org/10.1021/ja802342m.

Shao, L.Y., Li, W.J., Yang, S.S., Shi, Z.B., Lü, S.L., 2007. Mineralogical characteristics of airborne particles collected in beijing during a severe asian dust storm period in spring 2002. Sci. China, ser. D Earth Sci. 50, 953–959. https://doi.org/10.1007/s11430-007-0035-7.

Shi, Z., Krom, M.D., Bonneville, S., Baker, A.R., Jickells, T.D., Benning, L.G., 2009. formation of iron nanoparticles and increase in iron reactivity in mineral dust during simulated cloud processing. Environ. Sci. Technol. 43, 6592–6596. https://doi.org/10.1021/es901294g.

Shi, Z., Krom, M.D., Jickells, T.D., Bonneville, S., Carslaw, K.S., Mihalopoulos, N., Baker, A.R., Benning, L.G., 2012. Impacts on iron solubility in the mineral dust by processes in the source region and the atmosphere: a review. Aeolian Res 5, 21–42. https://doi.org/10.1016/j.aeolia.2012.03.001.

Shkrob, I.A., Marin, T.W., Chemerisov, S.D., Wishart, J.F., 2011. Radiation and radical chemistry of NO_3^- , HNO_3 , and dialkylphosphoric acids in room-temperature ionic liquids. J. Phys. Chem. B 115, 10927–10942. https://doi.org/10.1021/jp206579j.

Skiles, S.M., Painter, T.H., Belnap, J., Holland, L., Reynolds, R.L., Goldstein, H.L., Lin, J., 2015. Regional variability in dust-on-snow processes and impacts in the upper Colorado river basin. Hydrol. Process. 29, 5397–5413. http://doi.org/10.1002/hyp.10569.

Stefánsson, A., 2007. Iron(III) hydrolysis and solubility at 25 °C. Environ. Sci. Technol. 41, 6117–6123. https://doi.org/10.1021/es070174h.

Stucki, J.W., 1981. The quantitative assay of minerals for Fe^{2+} and Fe^{3+} using 1,10-phenanthroline; sources of variability. Soil Sci. Soc. Am. J. 45, 638–641. https://doi.org/10.2136/sssaj1981.03615995004500030039x.

Su, H., Cheng, Y., Oswald, R., Behrendt, T., Trebs, I., Meixner, F.X., Andreae, M.O., Cheng, P., Zhang, Y., Pöschl, U., 2011. Soil nitrite as a source of atmospheric HONO and OH radicals. Science 333, 1616–1618. https://doi.org/10.1126/science.1207687.

Tyrrell, T., Merico, A., Waniek, J.J., Wong, C.S., Metzl, N., Whitney, F., 2005. Effect of seafloor depth on phytoplankton blooms in high-nitrate, low-chlorophyll (HNLC) regions. J. Geophys. Res. Biogeosciences 110, 1–12. https://doi.org/10.1029/2005JG000041.

Vainer, S., Erel, Y., Matmon, A., 2018. Provenance and depositional environments of quaternary sediments in the southern Kalahari basin. Chem. Geol. 476, 352–369. https://doi.org/10.1016/j.chemgeo.2017.11.031.

Van Gosen, B.S., Ellefsen, K.J., 2018. Titanium mineral resources in heavy-mineral sands in the atlantic coastal plain of the Southeastern United States. U.S. Geological Survey Scientific Investigations Report 2018–5045. pp. 32. https://doi.org/10.3133/sir20185045.

Wang, Q., Zhu, C., Yun, J., Hu, Q., Yang, G., 2018. Compositional transformations as well as thermodynamics and mechanism of dissolution for clay minerals. Chem. Geol. 494, 109–116. https://doi.org/10.1016/j.chemgeo.2018.07.024.

Wiederhold, J.G., Kraemer, S.M., Teutsch, N., Borer, P.M., Halliday, A.N., Kretzschmar, R., 2006. Iron isotope fractionation during proton-promoted, ligand-controlled, and reductive dissolution of goethite. Environ. Sci. Technol. 40, 3787–3793. https://doi.org/10.1021/es052228y.

Wijenayaka, L.A., Rubasinghege, G., Baltrusaitis, J., Grassian, V.H., 2012. Surface chemistry of α-FeOOH nanorods and microrods with gas-phase nitric acid and water vapor: insights into the role of particle size, surface structure, and surface hydroxyl groups in the adsorption and reactivity of α-FeOOH with atmospheric gases. J. Phys. Chem. C 116, 12566–12577. https://doi.org/10.1021/jp301139x.

Wild, R.J., Edwards, P.M., Bates, T.S., Cohen, R.C., De Gouw, J.A., Dubé, W.P., Gilman, J.B., Holloway, J., Kercher, J., Koss, A.R., Lee, L., Lerner, B.M., McLaren, R., Quinn, P.K., Roberts, J.M., Stutz, J., Thornton, J.A., Veres, P.R., Warneke, C., Williams, E., Young, C.J., Yuan, B., Zarzana, K.J., Brown, S.S., 2016. Reactive nitrogen partitioning and its relationship to winter ozone events in Utah. Atmos. Chem. Phys. 16, 573–583. https://doi.org/10.5194/acp-16-573-2016.

Wu, J., Rember, R., Cahill, C., 2007. Dissolution of aerosol iron in the surface waters of the north pacific and North atlantic oceans as determined by a semicontinuous flow-through reactor method. Glob. Biogeochem. Cycles 21, 1–10. https://doi.org/10.1029/2006GB002851.

Xing, W., Liu, G., 2011. Iron biogeochemistry and its environmental impacts in freshwater lakes. Fresen 20, 1339–1345.

Xiong, L. Bin, Li, J.L., Yang, B., Yu, Y., 2012. Ti^{3+} in the surface of titanium dioxide: generation, properties and photocatalytic application. J. Nanomater. 2012, 1–13. https://doi.org/10.1155/2012/831524.

Yoshida, A., Ohata, S., Moteki, N., Adachi, K., Mori, T., Koike, M., Takami, A., 2018. Abundance and emission flux of the anthropogenic iron oxide aerosols from the east asian Continental outflow. J. Geophys. Res. Atmos. 123 11,194-11,209. https://doi.org/10.1029/2018JD028665.

Yu, Y., Dunlop, D.J., Özdemir, Ö., 2002. Partial anhysteretic remanent magnetization in magnetite. J. Geophys. Res. Solid Earth 107, 1–9. https://doi.org/10.1029/2001JB001269.

Zhang, J., Nosaka, Y., 2014. Mechanism of the OH radical generation in photocatalysis with TiO_2 of different crystalline types. J. Phys. Chem. C 118, 10824–10832. https://doi.org/10.1021/jp501214m.

Zhang, X., Zhao, L., Tong, D.Q., Wu, G., Dan, M., Teng, B., 2016. A systematic review of global Desert dust and associated human health effects. Atmosphere 158, 1–30. https://doi.org/10.3390/atmos7120158.

Zhang, Z., Goldstein, H.L., Reynolds, R.L., Hu, Y., Wang, X., Zhu, M., 2018. Phosphorus speciation and solubility in aeolian dust deposited in the interior American west. Environ. Sci. Technol. 52, 2658–2667. https://doi.org/10.1021/acs.est.7b04729.

Zhu, X., Prospero, J.M., Savoie, D.L., Millero, F.J., Zika, R.G., Saltzman, E.S., 1993. Photoreduction of iron(III) in marine mineral aerosol solutions. J. Geophys. Res. Atmos. 98, 9039–9046. https://doi.org/10.1029/93JD00202.